INTERNATIONAL JOURNAL OF
NUMERICAL ANALYSIS AND MODELING
Volume 6, Number 2, Pages 193–216

DEVELOPMENT OF A *hp*-LIKE DISCONTINUOUS GALERKIN TIME-DOMAIN METHOD ON NON-CONFORMING SIMPLICIAL MESHES FOR ELECTROMAGNETIC WAVE PROPAGATION

HASSAN FAHS

(Communicated by Jun Zou)

Abstract. This work is concerned with the design of a *hp*-like discontinuous Galerkin (DG) method for solving the two-dimensional time-domain Maxwell equations on non-conforming locally refined triangular meshes. The proposed DG method allows non-conforming meshes with arbitrary-level hanging nodes. This method combines a centered approximation for the evaluation of fluxes at the interface between neighboring elements of the mesh, with a leap-frog time integration scheme. It is an extension of the DG formulation recently studied in [13]. Several numerical results are presented to illustrate the efficiency and the accuracy of the method, but also to discuss its limitations, through a set of 2D propagation problems in homogeneous and heterogeneous media.

Key Words. Maxwell's equations, discontinuous Galerkin method, *hp*-like method, non-conforming triangular mesh, computational electromagnetism.

1. Introduction

The difficulties linked to the numerical solution of the time-domain Maxwell equations find their roots in the characteristics of the underlying wave propagation problems, *i.e.* the geometry of the diffracting objects, the physical features of the propagation medium (heterogeneity, physical dispersion and dissipation) and the type of sources (wires, etc.). Applications with such characteristics can be found throughout the applied sciences and engineering, *e.g.* the design and optimization of antennas [5] and radars [21], the design of emerging technologies such as high speed electronics and integrated optics, and a variety of military and civilian applications [22]-[20]. Other challenging applications are addressing societal questions such as the potential adverse effects of electromagnetic waves emitted by mobile phones [24]. Such problems require high fidelity approximate solutions with a rigorous control of the numerical errors. Even for linear problems such conditions force one to look beyond standard computational techniques and seek new numerical frameworks enabling the accurate, efficient, and robust modeling of wave phenomena over long simulation times in settings of realistic geometrical complexity.

The finite difference time-domain (FDTD) method, first introduced by Yee in 1966 [33] and later developed by Taflove and others [28], has been used for a broad range of applications in computational electromagnetics. In spite of its flexibility and second-order accuracy in a homogeneous medium, the Yee scheme suffers from serious accuracy degradation when used to model curved objects or when treating material interfaces. Indeed, the so-called staircasing approximation may

Received by the editors March 06, 2008 and, in revised form, October 29, 2008.
2000 *Mathematics Subject Classification.* 65M50, 65M60, 78A25, 78A45.

lead to local zeroth-order and at most first-order accuracy; it may also produce locally non-convergent results [11]. Furthermore, for Maxwell's equations with discontinuous coefficients, the Yee scheme might not be able to capture the possible discontinuity of the solution across the interfaces [11]. A number of finite difference methods have been proposed in the past for the treatment of curved interfaces. The usual and straightforward approach is to introduce local modification into the Yee scheme but still keep the staggered grid [12]-[31], or to use local mesh refinements [9]. Recently, some studies have been concerned with high-order embedded FDTD schemes in the presence of material interfaces [16], including the staggered fourth-order accurate methods by Yefet *et al.* [29]-[34], and the fourth-order orthogonal curvilinear staggered grid methods by Xie *et al.* [32]. Also, high-order FDTD methods via hierarchical implicit derivative matching are presented in [36]. Most of these methods, however, have not really penetrated into main stream user community, partly due to their complicated nature and partly because these new methods themselves often introduce other complications.

Finite element methods can handle unstructured meshes and complex geometries but the development of such methods for solving Maxwell's equations, especially those with high-order accuracy, has been relatively slow. A primary reason is the appearance of spurious, non-physical solutions when a straightforward nodal continuous Galerkin finite element scheme is used to approximate the Maxwell curl-curl equations. Bossavit made the fundamental observation that the use of special curl-conforming elements [19] would overcome the problem of spurious modes by mimicking properties of vector algebra [3]. Although very successful, such formulations are not entirely void of problems: the algebraic problems are larger than for nodal elements and the conformity requirements of the continuous Galerkin formulation makes adaptivity a complex task.

In an attempt to offer an alternative to the classical finite element formulation based on edge elements, we consider here discontinuous Galerkin formulations [6] based on high-order nodal interpolation for solving the time-domain Maxwell equations in first-order form. Discontinuous Galerkin time-domain (DGTD) methods based on discontinuous finite element spaces, easily handle elements of various types and shapes, irregular non-conforming meshes [13], and even locally varying polynomial degree, and hence offer great flexibility in the mesh design. They also lead to (block-) diagonal mass matrices and therefore yield fully explicit, inherently parallel methods when coupled with explicit time stepping [2]. In fact, for constant material coefficients, the mass matrix is diagonal for a judicious choice of (locally orthogonal) shape functions [23]. Moreover, continuity is weakly enforced across mesh interfaces by adding suitable bilinear forms (so-called numerical fluxes) to the standard variational formulations. Whereas high-order discontinuous Galerkin time-domain methods have been developed on conforming hexahedral [8] and tetrahedral [14]-[15] meshes, the design of non-conforming discontinuous Galerkin time-domain methods is still in its infancy. In practice, the non-conformity can result from a local refinement of the mesh (*i.e.* h-refinement), of the interpolation degree (*i.e.* p-enrichment) or of both of them (*i.e.* hp-refinement).

This work is a continuation of [13] where a h-refinement DGTD-$\mathbb{P}_p$ method was introduced for solving the two-dimensional time-domain Maxwell equations on non-conforming triangular meshes. The remaining of this paper is organized as follows. In section 2 we recall the basic features of the discontinuous Galerkin time-domain formulation for solving the two-dimensional Maxwell equations in first-order form, based on totally centered numerical fluxes and a leap-frog time-integration scheme.

The *hp*-like DGTD method is presented in section 3. In this section we also assess, through a simple example, the numerical dispersion properties of the *hp*-like DGTD method. We show that the proposed *hp*-like method can effectively suppress numerical dispersion caused by the low order DGTD-$\mathbb{P}_p$ ($p = 0, 1$) method. The *hp*-like DGTD method is evaluated numerically in section 4, in terms of accuracy, efficiency, numerical convergence and overall performance. Moreover, a comparison between the conforming and non-conforming DGTD methods is accomplished. Finally, section 5 concludes this paper and states future research directions.

2. Discontinuous Galerkin Time-Domain method

We shall consider the solution of the two-dimensional Maxwell equations for a z-transverse magnetic (TM) polarization on a bounded domain $\Omega \subset \mathbb{R}^2$:

$$\begin{cases} \epsilon \dfrac{\partial E_z}{\partial t} - \dfrac{\partial H_y}{\partial x} + \dfrac{\partial H_x}{\partial y} = 0, \\ \mu \dfrac{\partial H_x}{\partial t} + \dfrac{\partial E_z}{\partial y} = 0, \\ \mu \dfrac{\partial H_y}{\partial t} - \dfrac{\partial E_z}{\partial x} = 0, \end{cases} \tag{2.1}$$

where the magnetic field $\mathbf{H} = {}^t(H_x, H_y, 0)$ is transverse to the z-direction and the electric field $\mathbf{E} = {}^t(0, 0, E_z)$ has only one component along the z-direction. The parameters ϵ and μ refer to the electric permittivity and magnetic permeability, respectively, of the materials. On the boundary $\Gamma = \partial\Omega$ we use either a perfect electric conductor (PEC) condition *i.e.* $E_z = 0$, or a first order Silver-Müller absorbing boundary condition *i.e.* $E_z = c\mu(n_y H_x - n_x H_y)$, or both of them, where $c = 1/\sqrt{\epsilon\mu}$ is the speed of propagation and $\vec{n} = (n_x, n_y)$ denotes the unit normal vector pointing outward to Γ.

We consider a partition $\mathcal{T}_h$ of Ω into a set of triangles T_i of size h_i with boundaries ∂T_i such that the mesh size $h = \max_{T_i \in \mathcal{T}_h} h_i$. To each $T_i \in \mathcal{T}_h$ we assign an integer $p_i \geq 0$ (the local interpolation order) and we collect the p_i in the vector $p = \{p_i : T_i \in \mathcal{T}_h\}$. Of course, if p_i is uniform in all element T_i of the mesh, we have $p = p_i$. Within this construction we admit meshes with possibly hanging nodes *i.e.* by allowing non-conforming (or irregular) meshes where element vertices can lie in the interior of edges of other elements (see Fig. 2.1). Each triangle T_i is assumed to be the image, under a smooth bijective (diffeomorphic) mapping τ_i, of a fixed reference triangle $\hat{\mathrm{T}} = \{\hat{x}, \hat{y} |\ \hat{x}, \hat{y} \geq 0; \hat{x} + \hat{y} \leq 1\}$. Assuming that T_i is a straight sided triangle defined through the coordinates of the three vertices $\mathbf{v}_1^i$, $\mathbf{v}_2^i$ and $\mathbf{v}_3^i$ (see Fig. 2.2), the correspondence between the two triangles $\hat{\mathrm{T}}$ and T_i is established through the use of the barycentric coordinates $(\lambda_1, \lambda_2, \lambda_3)$. We recall that any point $\mathbf{x}^i \in T_i$ can be expressed as a convex combination of the vertices of T_i and the mapping is simply given by $\tau_i : (\hat{x}, \hat{y}) \in \hat{\mathrm{T}} \to \mathbf{x}^i$, such that $\mathbf{x}^i(\hat{x}, \hat{y}) = \lambda_1 \mathbf{v}_1^i + \lambda_2 \mathbf{v}_2^i + \lambda_3 \mathbf{v}_3^i$, where $\lambda_1 + \lambda_2 + \lambda_3 = 1$ and $0 \leq (\lambda_1, \lambda_2, \lambda_3) \leq 1$ with $\lambda_1 = 1 - \hat{x} - \hat{y},\ \lambda_2 = \hat{x}$ and $\lambda_3 = \hat{y}$.

In the following, for a given partition $\mathcal{T}_h$ and vector p, we seek approximate solutions to (2.1) in the finite dimensional subspace $V_p(\mathcal{T}_h) := \{v \in L^2(\Omega) : v_{|T_i} \in \mathbb{P}_{p_i}(T_i)\ ,\ \forall T_i \in \mathcal{T}_h\}$, where $\mathbb{P}_{p_i}(T_i)$ denotes the space of nodal polynomials $\{\varphi_{ij}\}_{j=1}^{d_i}$ of total degree at most p_i in the element T_i. The space $V_p(\mathcal{T}_h)$ has the dimension d_i, the local number of degrees of freedom. Note that the polynomial degree, p_i, may vary from element to element in the mesh and that a function $v_h^p \in V_p(\mathcal{T}_h)$ is discontinuous across element interfaces. For each triangle T_i, ϵ_i and μ_i respectively

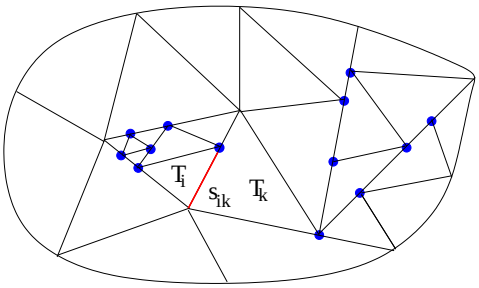

FIGURE 2.1. Irregular mesh with hanging nodes.

denote the local constant electric permittivity and magnetic permeability. For two neighboring triangles T_i and T_k in $\mathcal{T}_h$, the (non-empty) intersection $T_i \cap T_k$ is an (oriented) edge s_{ik} which we will call *interface*, with oriented normal vector $\vec{n}_{ik}$ and with unitary one $\vec{\widetilde{n}}_{ik}$. For the boundary interfaces, the index k corresponds to a fictitious element outside the domain. By non-conforming interface we mean an interface s_{ik} which is such that at least one of its two vertices is a hanging node, or/and such that $p_{i|_{s_{ik}}} \neq p_{k|_{s_{ik}}}$. Finally, we denote by $\mathcal{V}_i$ the set of indices of the neighbors elements of T_i.

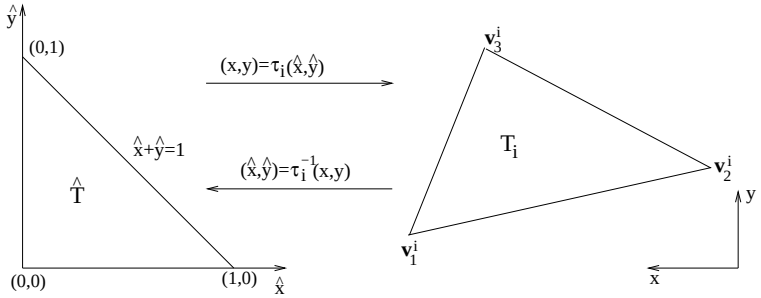

FIGURE 2.2. Mapping between the physical triangle T_i and the master triangle $\hat{\mathrm{T}}$.

We now derive the spatial discretization. Taking the product of system (2.1) by a given basis function $\varphi_{ij} \in \mathbb{P}_{p_i}(T_i), 1 \leq j \leq d_i$, and integrating over T_i yields :

$$
\left\{
\begin{array}{lcll}
\displaystyle\int_{T_i} \epsilon_i \frac{\partial E_z}{\partial t}\varphi_{ij} & + & \displaystyle\int_{T_i} H_y \frac{\partial \varphi_{ij}}{\partial x} - \int_{T_i} H_x \frac{\partial \varphi_{ij}}{\partial y} & \\
 & - & \displaystyle\int_{\partial T_i} H_y \varphi_{ij} \widetilde{n}_{ikx} + \int_{\partial T_i} H_x \varphi_{ij} \widetilde{n}_{iky} & = 0, \\
\displaystyle\int_{T_i} \mu_i \frac{\partial H_x}{\partial t}\varphi_{ij} & - & \displaystyle\int_{T_i} E_z \frac{\partial \varphi_{ij}}{\partial y} + \int_{\partial T_i} E_z \varphi_{ij} \widetilde{n}_{iky} & = 0, \\
\displaystyle\int_{T_i} \mu_i \frac{\partial H_y}{\partial t}\varphi_{ij} & + & \displaystyle\int_{T_i} E_z \frac{\partial \varphi_{ij}}{\partial y} - \int_{\partial T_i} E_z \varphi_{ij} \widetilde{n}_{ikx} & = 0.
\end{array}
\right. \tag{2.2}
$$

For any field $\mathrm{X} \in \{E_z, H_x, H_y\}$, we denote by X_i the L^2-projection on the linear space $\mathsf{Span}\{\varphi_{ij},\ 1 \leq j \leq d_i\}$ spanned by functions defined on T_i, and where $\{\varphi_{ij}\}_{j=1,\ldots,d_i} \in \mathbb{P}_{p_i}(T_i)$ is a family of linearly independent functions. In each triangle T_i we construct a polynomial representation of the magnetic and electric fields

and for simplicity and efficiency reasons we adopt a Lagrangian interpolation approach based on a set of nodes defined on the master (reference) triangle $\hat{\mathrm{T}}$ [26]. Using this notation, we have the following global discontinuous representation of the field:

$$\mathrm{X} \simeq \sum_i \mathrm{X}_i(t,x,y) = \sum_i \sum_{j=1}^{d_i} X_{ij}(t)\varphi_{ij}(x,y), \tag{2.3}$$

where X_{ij} is the jth degree of freedom of the field X_i. We denote by $\mathbf{X}_i$ the column vector $(X_{ij})_{1\leq j\leq d_i}$. The approximation field $\mathrm{X}_h \in \{(E_z)_h, (H_x)_h, (H_y)_h\}$, defined by $(\mathrm{X}_{h|T_i} = \mathrm{X}_i, \forall i)$ is allowed to be discontinuous across element boundaries and, for such a discontinuous field X_h, we define its average $\{\mathrm{X}_h\}_{ik}$ on any internal face s_{ik}, as:

$$\{\mathrm{X}_h\}_{ik} = \frac{\mathrm{X}_{i|s_{ik}} + \mathrm{X}_{k|s_{ik}}}{2}. \tag{2.4}$$

Note that for any internal face s_{ik}, $\{\mathrm{X}_h\}_{ik} = \{\mathrm{X}_h\}_{ki}$. For any integral over ∂T_i, a specific treatment must be introduced since the approximate fields are discontinuous through element faces. We choose to use a centered approximation:

$$\forall i, \forall k \in \mathcal{V}_i,\ \mathrm{X}_{|s_{ik}} \simeq \{\mathrm{X}_h\}_{ik}. \tag{2.5}$$

For what concerns time discretization, we propose to use a leap-frog time integration scheme which has both the advantage to be explicit and free of time dissipation. In the sequel, superscripts refer to time stations and Δt is the fixed time-step. The unknowns related to the electric field are approximated at integer time stations $t^n = n\Delta t$ and are denoted by $\mathbf{E}^n_{z_i}$. The unknowns related to the magnetic field are approximated at half-integer time stations $t^{n+\frac{1}{2}} = (n+\frac{1}{2})\Delta t$ and are denoted by $\mathbf{H}^{n+\frac{1}{2}}_{x_i}$ and $\mathbf{H}^{n+\frac{1}{2}}_{y_i}$.

The boundary conditions on Γ are treated in a weak sense by defining some values for the fields E_z, H_x and H_y in the fictitious neighboring element T_k. The treatment of boundary conditions is weak in the sense that the traces on $s_{ik} \in \Gamma$ of fictitious fields $\mathbf{E}^n_{z_k}, \mathbf{H}^{n+\frac{1}{2}}_{x_k}$ and $\mathbf{H}^{n+\frac{1}{2}}_{y_k}$ are used for the computation of numerical fluxes for the boundary element T_i. More precisely, for a metallic boundary interface s_{ik}, the fictitious values are chosen as :

$$\forall (x,y) \in s_{ik} : \begin{cases} \mathbf{H}^{n+\frac{1}{2}}_{x_k}(x,y) = \mathbf{H}^{n+\frac{1}{2}}_{x_i}(x,y),\ \mathbf{H}^{n+\frac{1}{2}}_{y_k}(x,y) = \mathbf{H}^{n+\frac{1}{2}}_{y_i}(x,y), \\ \mathbf{E}^n_{z_k}(x,y) = -\mathbf{E}^n_{z_i}(x,y), \end{cases} \tag{2.6}$$

and for an absorbing boundary interface s_{ik}, the fictitious values are :

$$\forall (x,y) \in s_{ik} :\ \mathbf{E}^{n+1}_{z_k}(x,y) = c_i\mu_i(n_{iky}\mathbf{H}^{n+\frac{1}{2}}_{x_i}(x,y) - n_{ikx}\mathbf{H}^{n+\frac{1}{2}}_{y_i}(x,y)). \tag{2.7}$$

The discontinuous Galerkin DGTD-$\mathbb{P}_{p_i}$ method can be written in the following matrix form:

$$
\left\{
\begin{array}{lcl}
\mathbb{M}_i^{\epsilon}\dfrac{\mathbf{E}_{z_i}^{n+1}-\mathbf{E}_{z_i}^{n}}{\Delta t} & = & -\mathbb{K}_i^{x}\mathbf{H}_{y_i}^{n+\frac{1}{2}}+\mathbb{K}_i^{y}\mathbf{H}_{x_i}^{n+\frac{1}{2}} \\
 & & +\displaystyle\sum_{k\in\mathcal{V}_i}\big(\mathbb{G}_{x_{ik}}^{n+\frac{1}{2}}-\mathbb{G}_{y_{ik}}^{n+\frac{1}{2}}\big), \\
\mathbb{M}_i^{\mu}\dfrac{\mathbf{H}_{x_i}^{n+\frac{1}{2}}-\mathbf{H}_{x_i}^{n-\frac{1}{2}}}{\Delta t} & = & \mathbb{K}_i^{y}\mathbf{E}_{z_i}^{n}-\displaystyle\sum_{k\in\mathcal{V}_i}\mathbb{F}_{y_{ik}}^{n}, \\
\mathbb{M}_i^{\mu}\dfrac{\mathbf{H}_{y_i}^{n+\frac{1}{2}}-\mathbf{H}_{y_i}^{n-\frac{1}{2}}}{\Delta t} & = & -\mathbb{K}_i^{x}\mathbf{E}_{z_i}^{n}+\displaystyle\sum_{k\in\mathcal{V}_i}\mathbb{F}_{x_{ik}}^{n},
\end{array}
\right. \tag{2.8}
$$

where the vector quantities $\mathbb{F}_{xik}^{n}, \mathbb{F}_{yik}^{n}, \mathbb{G}_{xik}^{n+\frac{1}{2}}$ and $\mathbb{G}_{yik}^{n+\frac{1}{2}}$ are defined as:

$$
\left\{
\begin{array}{lll}
\mathbb{F}_{x_{ik}}^{n}=\mathbb{S}_{ik}^{x}\mathbf{E}_{z_k}^{n} & , & \mathbb{F}_{y_{ik}}^{n}=\mathbb{S}_{ik}^{y}\mathbf{E}_{z_k}^{n}, \\
\mathbb{G}_{x_{ik}}^{n+\frac{1}{2}}=\mathbb{S}_{ik}^{x}\mathbf{H}_{y_k}^{n+\frac{1}{2}} & , & \mathbb{G}_{y_{ik}}^{n+\frac{1}{2}}=\mathbb{S}_{ik}^{y}\mathbf{H}_{x_k}^{n+\frac{1}{2}},
\end{array}
\right. \tag{2.9}
$$

and the positive definite symmetric mass matrices $\mathbb{M}_i^{\epsilon}$, $\mathbb{M}_i^{\mu}$, and the skew-symmetric stiffness matrix $\mathbb{K}_i^{\mathbf{x}},\ \mathbf{x}\in\{x,y\}$ (all of size $d_i\times d_i$) are given by:

$$
\left\{
\begin{array}{l}
(\mathbb{M}_i^{\epsilon})_{jl}=\displaystyle\int_{T_i}\epsilon_i\varphi_{ij}\varphi_{il}, \quad (\mathbb{M}_i^{\mu})_{jl}=\int_{T_i}\mu_i\varphi_{ij}\varphi_{il}, \\
(\mathbb{K}_i^{\mathbf{x}})_{jl}=\dfrac{1}{2}\displaystyle\int_{T_i}\Big(\frac{\partial\varphi_{ij}}{\partial\mathbf{x}}\varphi_{il}-\varphi_{ij}\frac{\partial\varphi_{il}}{\partial\mathbf{x}}\Big).
\end{array}
\right. \tag{2.10}
$$

For any interface s_{ik}, the $d_i\times d_k$ rectangular interface matrix $\mathbb{S}_{ik}^{\mathbf{x}},\ \mathbf{x}\in\{x,y\}$ is given by:

$$
(\mathbb{S}_{ik}^{\mathbf{x}})_{jl}=\frac{1}{2}\widetilde{n}_{ik\mathbf{x}}\int_{s_{ik}}\varphi_{ij}\varphi_{kl}. \tag{2.11}
$$

For any interface matrix $\mathbb{S}_{ik}^{\mathbf{x}}$, we have the following properties:

- if s_{ik} is an internal interface of the mesh then ${}^{t}\mathbb{S}_{ik}^{\mathbf{x}}=-\mathbb{S}_{ki}^{\mathbf{x}}$,
- if s_{ik} is a metallic boundary interface of the mesh then ${}^{t}\mathbb{S}_{ik}^{\mathbf{x}}=\mathbb{S}_{ik}^{\mathbf{x}}$.

Note that, if s_{ik} is a conforming interface, the matrix $\mathbb{S}_{ik}^{\mathbf{x}}$ can be evaluated in a direct way once and for all. However, if s_{ik} is a non-conforming interface, we cannot calculate this matrix with an exact formula because it strongly depends on the number of hanging nodes on the interface s_{ik}. For that, and only for non-conforming interfaces, we calculate the matrix $\mathbb{S}_{ik}^{\mathbf{x}}$ by using a Gaussian quadrature formula.

2.1. Stability and convergence analysis. We define the following discrete electromagnetic energy:

$$
\mathcal{E}^{n}=\frac{1}{2}\sum_{i}\big({}^{t}\mathbf{E}_{z_i}^{n}\mathbb{M}_i^{\epsilon}\mathbf{E}_{z_i}^{n}\ +\ {}^{t}\mathbf{H}_{x_i}^{n-\frac{1}{2}}\mathbb{M}_i^{\mu}\mathbf{H}_{x_i}^{n+\frac{1}{2}}\ +\ {}^{t}\mathbf{H}_{y_i}^{n-\frac{1}{2}}\mathbb{M}_i^{\mu}\mathbf{H}_{y_i}^{n+\frac{1}{2}}\big). \tag{2.12}
$$

The stability of the discontinuous Galerkin DGTD-$\mathbb{P}_{p_i}$ method (2.8)-(2.9) has been studied in [13] for non-conforming meshes and any local polynomial degree p_i on T_i. The method is conditionally stable under a CFL-like condition on the

time-step Δt which depends on p_i and on the level of hanging nodes. The basic idea is to prove that the energy (2.12) is a quadratic form who plays the role of a Lyapunov function of the whole set of numerical unknowns. The CFL condition is defined as follows (for more details we refer the reader to [13]) :

$$\forall i, \forall k \in \mathcal{V}_i, c_i \Delta t(2\alpha_i + \beta_{ik}) \leq 4 \min(\frac{|T_i|}{P_i^x}, \frac{|T_i|}{P_i^y}), \tag{2.13}$$

where c_i is the local speed of propagation, $|T_i|$ is the surface of T_i and $P_i^{\mathbf{x}} = \sum_{k \in \mathcal{V}_i} |n_{ik\mathbf{x}}|$. The constants α_i and β_{ik} ($k \in \mathcal{V}_i$) verify some inequalities [13] on T_i and s_{ik} :

$$\begin{cases} \forall \xi_i \in \mathsf{Span}\{\varphi_{ij}, 1 \leq j \leq d_i\}, \ \mathbf{x} \in \{x, y\} \\ \left\| \dfrac{\partial \xi_i}{\partial \mathbf{x}} \right\|_{T_i} \leq \dfrac{\alpha_i P_i^{\mathbf{x}}}{|T_i|} \|\xi_i\|_{T_i}, \quad \|\xi_i\|_{s_{ik}}^2 \leq \beta_{ik} \dfrac{\|\vec{n}_{ik}\|}{|T_i|} \|\xi_i\|_{T_i}^2. \end{cases}$$

The values of α_i only depend on the local polynomial order p_i while the values of β_{ik} depend on p_i and on the number of hanging nodes on the interface s_{ik}. Consequently, if p_i and the number of hanging nodes increase, the theoretical CFL values following (2.13) become restrictive [13]. We report here on the CFL values evaluated numerically (*i.e.* by assessing the limit beyond which we observe a growth of the discrete energy). The corresponding values of $\mathrm{CFL}_{p_i}^{\mathrm{num}}$ are summarized in Table 2.1 for the DGTD-$\mathbb{P}_p$ method.

Interpolation order p_i=p	**0**	**1**	**2**	**3**	**4**
Numerical CFL value $\mathrm{CFL}_p^{\mathrm{num}}$	1.0	0.3	0.2	0.1	0.08

TABLE 2.1. Numerical CFL of the DGTD-$\mathbb{P}_p$ method.

Convergence analysis. A theoretical convergence analysis of the DGTD-$\mathbb{P}_{p_i}$ method is conducted in [14], in the case of conforming simplicial meshes and $p_i = p$ everywhere. It is shown that the convergence order in space and time is:

$$\mathcal{O}(Th^{\min(s,p)}) + \mathcal{O}(\Delta t^2), \tag{2.14}$$

where Δt is the fixed time step over the interval $[0, T]$ and the solution belongs to $H^s(\Omega)$ with $s > 1/2$ a regularity parameter. In section 4 our attention is turned out the validity of this result in the case of non-conforming meshes using the DGTD-$\mathbb{P}_p$ and hp-like methods, and an answer is given here on the basis of numerical simulations.

3. hp-like discontinuous Galerkin method

We propose here a hp-like DGTD method where we combine h-refinement and p-enrichment strategies. In [13], a numerical dispersion has been observed when a low order conforming DGTD-$\mathbb{P}_p$ ($p = 0, 1$ and $p_i = p$ everywhere) is applied. This dispersion error is not reduced notably by using a h-refinement strategy (*i.e.* modifying h for a fixed p, yielding non-conforming locally refined meshes). On the other hand, the dispersion error is minimized when a p-enrichment strategy (*i.e.* modifying p for a fixed h) is used. However, the latter approach requires a large number of degrees of freedom and thus, increases substantially the computing time and memory usage. The method proposed here consists in using a high polynomial degree in the coarse (*i.e.* not refined) mesh and a low polynomial degree in the

refined region. The main objectives of the resulting *hp*-like DGTD method are to eliminate or to strongly reduce the dispersion error, and to decrease the computational cost. The resulting scheme is referred to as a DGTD-$\mathbb{P}_{p_c}$:$\mathbb{P}_{p_f}$ method , where p_c and p_f are the polynomial degrees in the coarse and fine elements respectively. If $p_c = p_f = p$, we recover the classical DGTD-$\mathbb{P}_p$ scheme studied in [13]. This kind of scheme is a first step towards a fully adaptive *hp*-refinement method relying on appropriate error estimators [7]. Fig. 3.1 shows two different representations of the fields, the first one using $\mathbb{P}_2$ and $\mathbb{P}_1$ approximations and the second one using $\mathbb{P}_3$ and $\mathbb{P}_0$ approximations. The stability of such a DGTD-$\mathbb{P}_{p_c}$:$\mathbb{P}_{p_f}$ method is ensured under some CFL conditions. In Table 3.1, we summarize the CFL conditions numerically observed for some polynomial degrees. These CFL conditions are to be compared with those obtained for the DGTD-$\mathbb{P}_p$ scheme (see Table 2.1). One can note that for $p_c = p_f + 1 = p + 1$, the DGTD-$\mathbb{P}_{p_c}$:$\mathbb{P}_{p_f}$ method has the same stability limit as the DGTD-$\mathbb{P}_p$ scheme, as long as the mesh is actually refined. This is not surprising, since the DGTD-$\mathbb{P}_{p_c}$ scheme, which has a reduced stability domain, is only used for elements of the coarse mesh (which are at least twice larger than elements of the refined mesh).

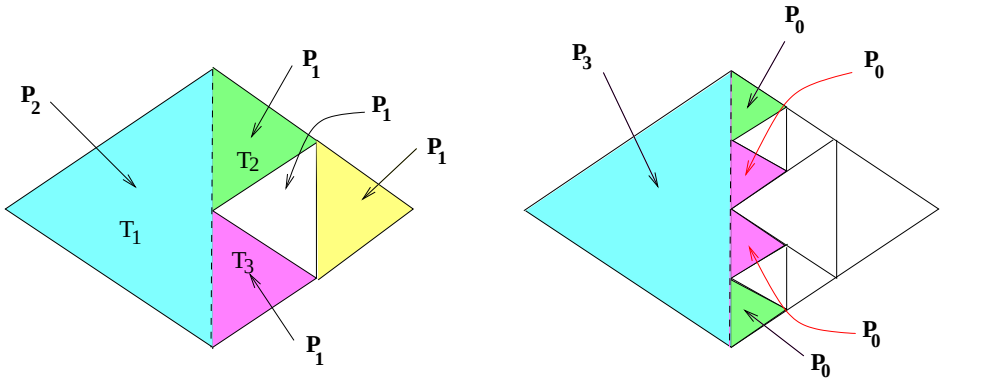

FIGURE 3.1. Fields representation examples.

Interpolation orders p_c:p_f	**1:0**	**2:0**	**3:0**	**2:1**	**3:1**	**3:2**	**4:2**	**4:3**
Numerical CFL value $\mathrm{CFL}^{\mathrm{num}}_{p_c:p_f}$	0.7	0.4	0.25	0.3	0.25	0.2	0.15	0.1

TABLE 3.1. Numerical CFL of the DGTD-$\mathbb{P}_{p_c}$:$\mathbb{P}_{p_f}$ method.

In order to demonstrate the ability of the DGTD-$\mathbb{P}_{p_c}$:$\mathbb{P}_{p_f}$ method to reduce the dispersion error with minimal cost, we consider the propagation of an eigenmode which is a standing wave of frequency $f = 212$ MHz and wavelength $\lambda = 1.4$ m in a unitary PEC cavity with $\epsilon = \mu = 1$ in normalized units. Owing to the existence of an exact analytical solution, this problem allows us to appreciate the numerical results at any point and time in the cavity. Numerical simulations make use of triangular meshes of the square $[0,1] \times [0,1]$ and non-conforming meshes are obtained by locally refining (three refinement levels) the square zone $[0.25, 0.75] \times [0.25, 0.75]$ as shown on Fig. 3.2.

Now, we aim at making a comparison between the DGTD-$\mathbb{P}_p$ method ($p_i = p$ everywhere) and the proposed DGTD-$\mathbb{P}_{p_c}$:$\mathbb{P}_{p_f}$ method. For this purpose, we use for

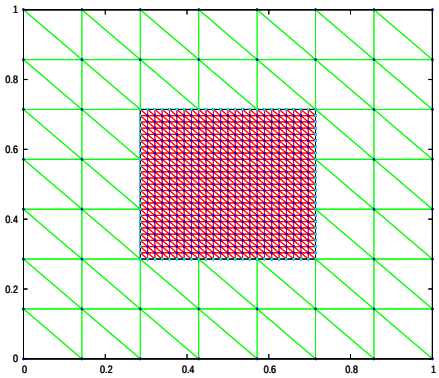

FIGURE 3.2. Non-conforming locally refined triangular mesh.

$p = 0, 1$ a non-conforming mesh consisting of 2304 triangles and 1233 nodes (112 of them are hanging nodes), and for $p \geq 2, \forall p_c, \forall p_f$ we use a non-conforming mesh consisting of 576 triangles and 329 (42 of them are hanging nodes). Results are shown on Fig. 3.3 in terms of time evolution of the approximate and exact values of the H_x component at a given point in the coarse grid (the five last periods of 43 are shown). One can see that the DGTD-$\mathbb{P}_p$ ($p \geq 2$) solutions compare very well with the exact one, but the DGTD-$\mathbb{P}_0$ and DGTD-$\mathbb{P}_1$ solutions exhibit a large dispersion error. Moreover, it can be seen from Fig. 3.3 that the DGTD-$\mathbb{P}_{p_c}$:$\mathbb{P}_{p_f}$ method do not introduce dispersion in the coarse grid where the CFL is far from optimal. Although the level of refinement is high, the coarse mesh is characterized by a few points per wavelength and the simulation is quite long. The time evolution of the L^2 error on the electromagnetic field $(\mathbf{E}, \mathbf{H})$ computed with the DGTD-$\mathbb{P}_p$ and DGTD-$\mathbb{P}_{p_c}$:$\mathbb{P}_{p_f}$ methods are plotted on Fig. 3.4. We can observe that the DGTD-$\mathbb{P}_{p_c}$:$\mathbb{P}_{p_f}$ ($\forall\ p_c, p_f$) method is, on one hand, more accurate (in terms of the L^2 error) than the low order DGTD-$\mathbb{P}_p$ ($p = 0, 1$) method and, on the other hand, comparable with the high-order DGTD-$\mathbb{P}_p$ ($p \geq 2$) method. We summarize in Table 3.2 the numbers of degrees of freedom (# dof) required by the DGTD-$\mathbb{P}_p$ and DGTD-$\mathbb{P}_{p_c}$:$\mathbb{P}_{p_f}$ methods.

DGTD-$\mathbb{P}_p$ method.					
p	**0**	**1**	**2**	**3**	**4**
# dof	2304	6912	3456	5760	8640
DGTD-$\mathbb{P}_{p_c}$:$\mathbb{P}_{p_f}$ method.					
p_c:p_f	**2:0**	**3:0**	**2:1**	**3:1**	**3:2**
# dof	896	1152	1920	2176	3712

TABLE 3.2. Eigenmode in a unitary PEC square cavity. # dof required by the DGTD-$\mathbb{P}_p$ and DGTD-$\mathbb{P}_{p_c}$:$\mathbb{P}_{p_f}$ methods using non-conforming meshes.

4. Numerical experiments

In this section, we consider several wave propagation problems in homogeneous and heterogeneous media for which analytical solutions exist. Our objectives are the following:

- to assess numerically and compare the convergence of the conforming and non-conforming DGTD methods,

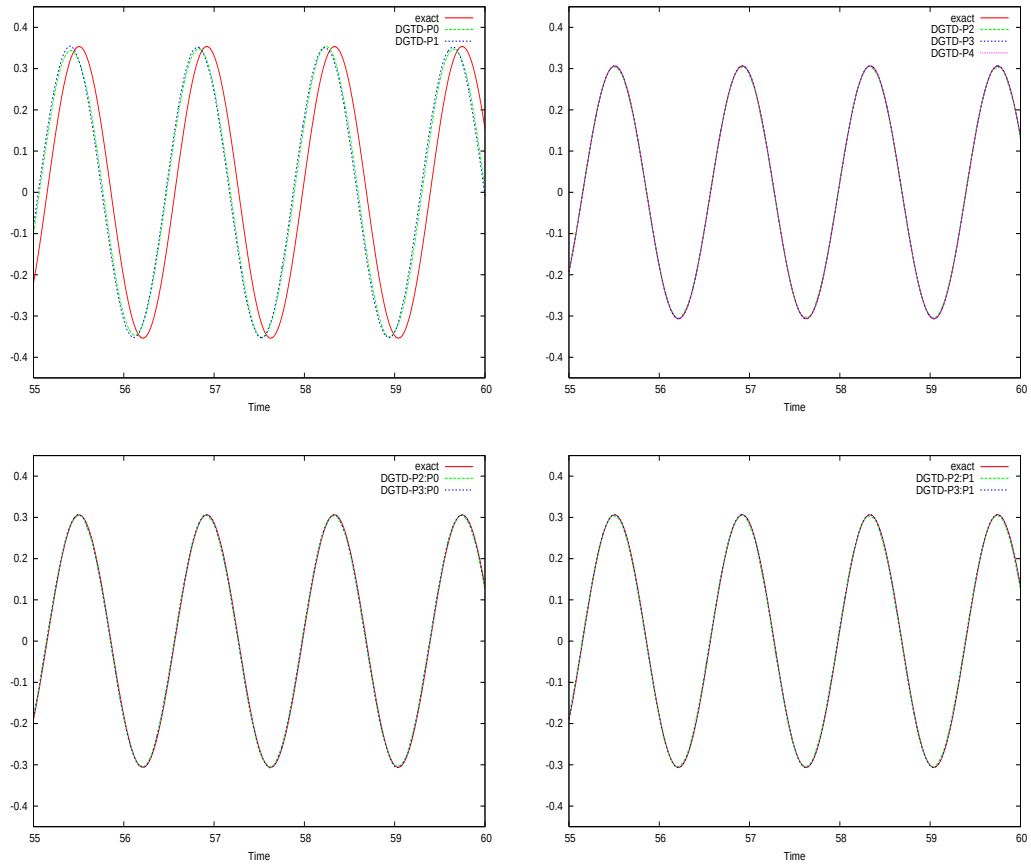

FIGURE 3.3. Eigenmode in a unitary PEC square cavity.
Time evolution of H_x: DGTD-$\mathbb{P}_p$ (top) and DGTD-$\mathbb{P}_{p_c}$:$\mathbb{P}_{p_f}$ (bottom).
Zoom on the last 4 periods.

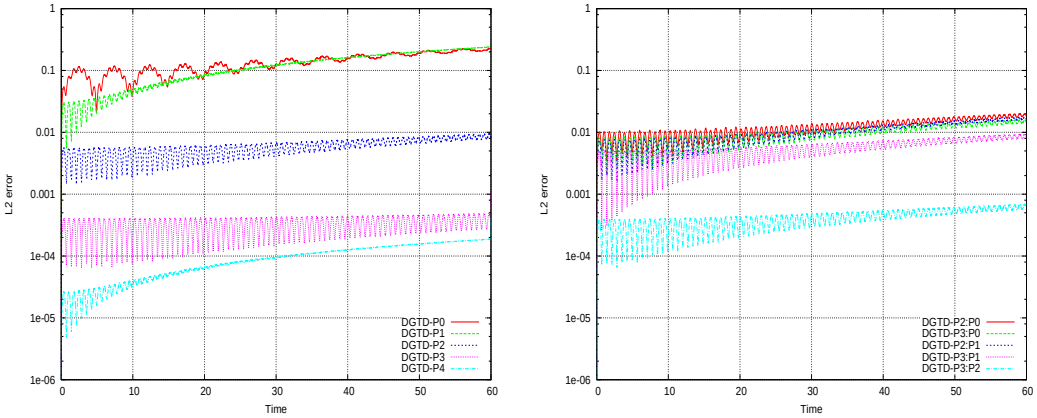

FIGURE 3.4. Eigenmode in a unitary PEC square cavity.
Time evolution of the L^2 error: DGTD-$\mathbb{P}_p$ (left) and DGTD-$\mathbb{P}_{p_c}$:$\mathbb{P}_{p_f}$ (right).

- to provide insights regarding the overall performance of the hp-refinement DGTD-$\mathbb{P}_{p_c}$:$\mathbb{P}_{p_f}$ method,
- to compare, on one hand, the conforming DGTD-$\mathbb{P}_p$ method with the non-conforming one and, on the other hand, the hp-refinement method with the h-refinement one.

4.1. Concentric PEC cylinders resonator. We consider a resonator which consists of two concentric PEC cylinders with an electromagnetic wave bouncing back and forth between the walls (see Fig. 4.1). The material is taken to be the vacuum *i.e.* $\epsilon = \mu = 1$ (relative quantities). The radii of the two cylinders are $r_1 = 1/6$ and $r_2 = 1/2$. The exact time-domain solution of the problem is [11]-[12] :

$$\begin{aligned}
E_z &= \cos(\omega t + \theta)[J_1(\omega r) + aY_1(\omega r)], \\
H_x &= -\frac{1}{2}\sin(\omega t + \theta)\sin(\theta)[J_0(\omega r) - J_2(\omega r) + a(Y_0(\omega r) - Y_2(\omega r))] \\
&\quad -\frac{\cos(\theta)}{\omega r}\cos(\omega t + \theta)[J_1(\omega r) + aY_1(\omega r)], \\
H_y &= \frac{1}{2}\sin(\omega t + \theta)\cos(\theta)[J_0(\omega r) - J_2(\omega r) + a(Y_0(\omega r) - Y_2(\omega r))] \\
&\quad -\frac{\sin(\theta)}{\omega r}\cos(\omega t + \theta)[J_1(\omega r) + aY_1(\omega r)],
\end{aligned}$$

for $r_1 < r < r_2$, where $(r,\ \theta) = (\sqrt{x^2 + y^2},\ \arctan(y/x))$ are the usual polar coordinates; J_n and Y_n stand for the n-th order Bessel functions of the first and second kind, respectively. The values of the parameters ω and a are obtained by enforcing the boundary condition $E_z = 0$ at $r = r_1$ and $r = r_2$. Then, as in [11], we set $\omega = 9.813695999428405$ and $a = 1.76368380110927$. First, a quasi-uniform conforming mesh is constructed (see Fig. 4.2 left). Then a non-conforming mesh is obtained by locally refining a cylindrical zone as shown on Fig. 4.2 right. Contour lines of the E_z and H_y components at time $t = 10$ are shown on Fig. 4.3 for a calculation based on the conforming DGTD-$\mathbb{P}_1$ method.

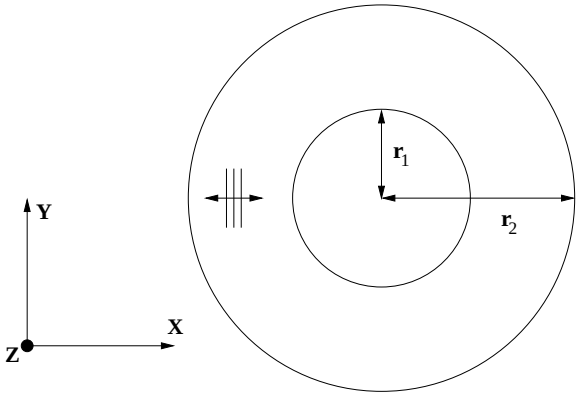

FIGURE 4.1. Concentric PEC cylinders resonator setting.

Two strategies are considered for this problem: the first one is the DGTD-$\mathbb{P}_p$ (or h-refinement) method using conforming and non-conforming meshes and the second one is the DGTD-$\mathbb{P}_{p_c}$:$\mathbb{P}_{p_f}$ (or hp-refinement) method using non-conforming meshes.

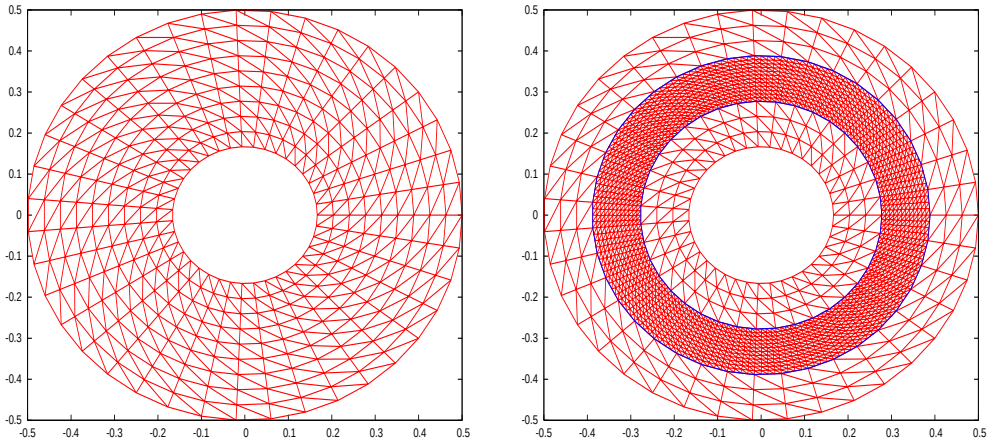

FIGURE 4.2. Concentric PEC cylinders resonator.
Example of conforming (left) and non-conforming (right) triangular meshes.

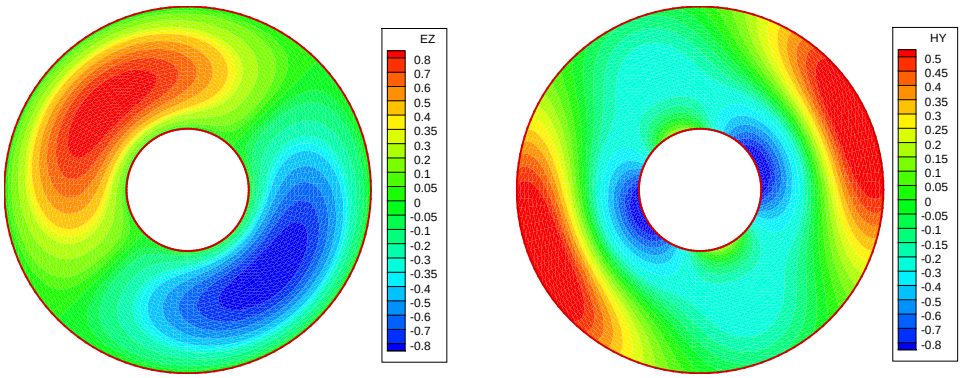

FIGURE 4.3. Concentric PEC cylinders resonator.
Contour lines of E_z (left) and H_y (right) at time $t = 10$.
DGTD-$\mathbb{P}_1$ method using a conforming mesh with 1088 nodes and 2048 triangles.

Fig. 4.4 and 4.5 illustrate respectively the numerical convergence of the DGTD-$\mathbb{P}_p$ and DGTD-$\mathbb{P}_{p_c}$:$\mathbb{P}_{p_f}$ methods using conforming and non-conforming triangular meshes, in terms of the evolution of the L^2 error as a function of the square root of the number of degrees of freedom. These errors are evaluated at time $t = 1$. Corresponding asymptotic convergence orders are summarized in Tables 4.1 and 4.2. As it could be expected from the use of a second-order accurate time integration scheme, the asymptotic convergence order is bounded above by 2 independently of the interpolation order p and higher order convergence orders will require more accurate time integration schemes. Furthermore, we can observe that for $p = 0, 1$, the convergence order is $\mathcal{O}(h^{p+1})$, and for $p_f = 0$ the convergence order of the DGTD-$\mathbb{P}_{p_c}$:$\mathbb{P}_{p_f}$ method is close to $\mathcal{O}(h^{1.5})$. From this point of view, the formula (2.14) is sub-optimal and leaves room for improvement in view of the development of p- and hp-adaptive DGTD methods.

Comparison with various FDTD methods. Here, we compare the DGTD-$\mathbb{P}_0$ method with two different FDTD schemes:

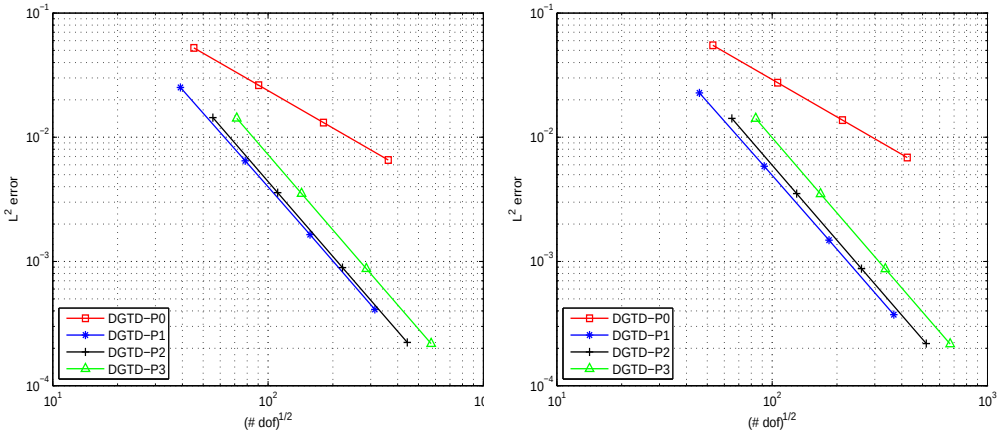

FIGURE 4.4. Concentric PEC cylinders resonator.
Numerical convergence of the h-refinement DGTD-$\mathbb{P}_p$ method.
Conforming (left) and non-conforming (right) triangular meshes.

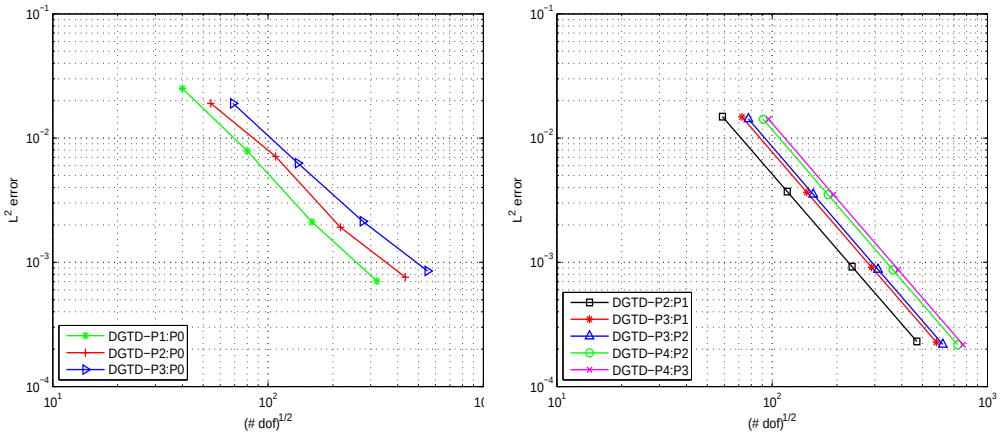

FIGURE 4.5. Concentric PEC cylinders resonator.
Numerical convergence of the hp-refinement DGTD-$\mathbb{P}_{p_c}$:$\mathbb{P}_{p_f}$ method.
Non-conforming triangular meshes.

DGTD-$\mathbb{P}_p$: Conforming triangular mesh.				
Interpolation order p	**0**	**1**	**2**	**3**
Convergence order	1.00	1.98	2.00	2.01
DGTD-$\mathbb{P}_p$: Non-conforming triangular mesh.				
Interpolation order p	**0**	**1**	**2**	**3**
Convergence order	1.00	1.98	2.01	2.01

TABLE 4.1. Numerical convergence of the DGTD-$\mathbb{P}_p$ method.

DGTD-$\mathbb{P}_{p_c}$:$\mathbb{P}_{p_f}$: Non-conforming triangular mesh.								
Interpolation orders p_c**:**p_f	**1:0**	**2:0**	**3:0**	**2:1**	**3:1**	**3:2**	**4:2**	**4:3**
Convergence order	1.72	1.55	1.50	2.00	2.00	2.01	2.01	2.01

TABLE 4.2. Numerical convergence of the DGTD-$\mathbb{P}_{p_c}$:$\mathbb{P}_{p_f}$ method.

(1) the classical second-order Yee scheme [33] staggered both in space and time where the numerical solution is carried out on a *staircased* mesh;
(2) a modification of Yee's scheme (referred to as Ty(2,4)), see [29]-[30], and chapter 2 in [28]. This method is fourth-order accurate in space and second-order accurate in time. The numerical solution is also computed on a stagger *staircased* mesh.

The L^2 error on the E_z component and the convergence rate of these two FDTD schemes evaluated at times $t = 1$ and $t = 10$ are given in Table 4.3. These results were taken from [1]-[32]. It is seen from Table 4.3 that the staircased FDTD approximation leads to an extremely slow convergence rate at early time ($t = 1$) and a divergent scheme at late time ($t = 10$). According to [32], this is probably not only because the staircasing misrepresents the shape of the cylinders, but also because of the fact that for this resonator case an electromagnetic wave is bouncing back and forth between the walls, so numerical errors accumulate quickly in the solution. These FDTD results are compared with the classical centered finite volume DGTD-$\mathbb{P}_0$ scheme on conforming triangular meshes. One can note that the DGTD-$\mathbb{P}_0$ conserves a linear convergence rate even for a long simulation time.

t=1			t=10		
Yee scheme (staircased) cartesian grid.					
Grid	L^2 error	Convergence rate	Grid	L^2 error	Convergence rate
1000	4.322E−01	–	1000	5.101E−01	–
4000	3.635E−01	0.28	4000	4.364E−01	0.23
16000	1.742E−01	1.06	16000	6.683E−01	−0.61
Ty(2,4) (staircased) cartesian grid.					
1000	4.038E−01	–	1000	2.642E−01	–
4000	3.347E−01	0.27	4000	7.079E−01	−1.42
16000	1.579E−01	1.08	16000	7.243E−01	−0.03
The classical centered finite volume DGTD-$\mathbb{P}_0$ scheme.					
$\sqrt{\text{dof}}$	L^2 error	Convergence rate	$\sqrt{\text{dof}}$	L^2 error	Convergence rate
90	2.62E−02	–	90	4.52E−02	–
180	1.31E−02	0.99	180	1.89E−02	1.25
360	6.65E−03	1.00	360	8.96E−03	1.08

TABLE 4.3. The L^2 errors on E_z for two different FDTD schemes and for the DGTD-$\mathbb{P}_0$ method.

4.2. Rectangular PEC resonator with material interface. We consider a problem in which a dielectric of relative permittivity ϵ_2 occupying the spatial region $[0, 0.5] \times [0, 1]$, is enclosed by a PEC-bounded $[0, 1.25] \times [0, 1]$ domain. The exact time-domain solution is [36] :

$$E_z = \begin{cases} \sin(a_1 x)\sin(\omega t)\sin(by), & 0 \le x \le \frac{1}{2}, \quad 0 \le y \le 1, \\ \cos(a_2 x)\sin(\omega t)\sin(by), & \frac{1}{2} \le x \le \frac{5}{4}, \quad 0 \le y \le 1, \end{cases}$$

$$H_x = \begin{cases} \frac{b}{\omega}\sin(a_1 x)\cos(\omega t)\cos(by), & 0 \le x \le \frac{1}{2}, \quad 0 \le y \le 1, \\ \frac{b}{\omega}\cos(a_2 x)\cos(\omega t)\cos(by), & \frac{1}{2} \le x \le \frac{5}{4}, \quad 0 \le y \le 1, \end{cases}$$

$$H_y = \begin{cases} -\frac{a_1}{\omega}\cos(a_1 x)\cos(\omega t)\sin(by), & 0 \le x \le \frac{1}{2}, \quad 0 \le y \le 1, \\ \frac{a_2}{\omega}\sin(a_2 x)\cos(\omega t)\sin(by), & \frac{1}{2} \le x \le \frac{5}{4}, \quad 0 \le y \le 1, \end{cases}$$

where $a_1^2 + b^2 = \epsilon_2\omega^2$, $a_2^2 + b^2 = \epsilon_1\omega^2$, $\sin(\frac{a_1}{2}) = \cos(\frac{a_2}{2})$ and $\cos(\frac{5a_2}{4}) = 0$. The values of the parameters appearing in these relations are defined by imposing the PEC condition on the boundary $x = 5/4$ and by ensuring the continuity of E_z across the material interface $x = 1/2$. As in [36]-[34], these parameter values are chosen as $\epsilon_1 = 1$, $\epsilon_2 = 2$, $a_1 = 3\pi$, $a_2 = 2\pi$, $b = \pi$, and $\omega = \sqrt{5}\pi$. The wavelength is $\lambda^{\epsilon_1} = 0.268$ in the air zone and $\lambda^{\epsilon_2} = 0.189$ in the dielectric zone, *i.e.* $\lambda^{\epsilon_1} \simeq 1.42\lambda^{\epsilon_2}$. Across the dielectric interface (*i.e.* the air/dielectric interface), the tangential components of the electromagnetic field E_z and H_y are continuous as well as their first y derivative. Furthermore, the first x derivative of E_z is continuous while that of H_y is discontinuous. Hence, the H_y component has a low regularity. An example plot of analytical solution is shown on Fig. 4.6.

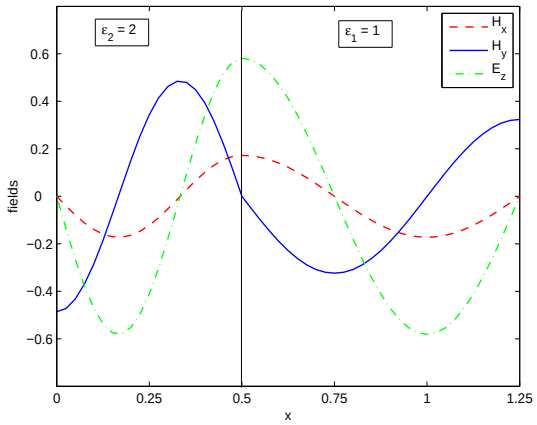

FIGURE 4.6. Rectangular PEC resonator with material interface. Plots of the analytical solution along the line $y = 3/4$ at time $t = 0.75$.

Numerical simulations make use of uniform triangular meshes such that the material interface $x = 1/2$ is aligned with the grid, *i.e.* the intersection between the interface $x = 1/2$ and $\text{int}(T_i)$ (the interior of T_i) is empty, $\forall$ triangle T_i of the mesh. The non-conforming meshes are obtained by locally refining the material region *i.e.* the zone $[0, 0.5] \times [0, 1]$. The overall numerical convergence of the DGTD-$\mathbb{P}_p$ and

DGTD-$\mathbb{P}_{p_c}$:$\mathbb{P}_{p_f}$ methods is respectively shown on Fig. 4.7 and 4.8 using conforming and non-conforming triangular meshes. Corresponding asymptotic convergence orders are listed in Tables 4.4 and 4.5. One can see that the convergence orders are lower than those observed with the previous test case, which is the result of the low regularity of the solution. Note that, the dielectric permittivity ϵ jumps at the dielectric interface and this discontinuity can significantly reduce the order of accuracy of the numerical methods particularly of the classical FDTD scheme. One can note here that the accuracy of the FDTD methods depend on the size of the jump in ϵ on the dielectric interface [18]. The strong point of the proposed DGTD methods is that the convergence order does not depend on the size of the jump in ϵ on the interface, it only depends on the regularity of the solution. We validate this by studying the convergence of the non-conforming DGTD-$\mathbb{P}_p$ method and using two different materials with $\epsilon_2 = 3.25$ and 6.625. Results in Table 4.6 show that the convergence order is always close to $\mathcal{O}(h^{(1)})$. This confirms that the convergence order of the proposed DGTD methods depends only on the regularity of the solution. To obtain higher convergence order, a special treatment of the numerical fluxes such as a regularization technique [18] can be used at the material interface. Table 4.7 shows the CPU times, the number of degrees of freedom and the number of time steps (# Δt) to achieve a prescribed error level. The results of the DGTD-$\mathbb{P}_{p_c}$:$\mathbb{P}_{p_f}$ on non-conforming meshes are very satisfactory comparing with those of the DGTD-$\mathbb{P}_p$ method.

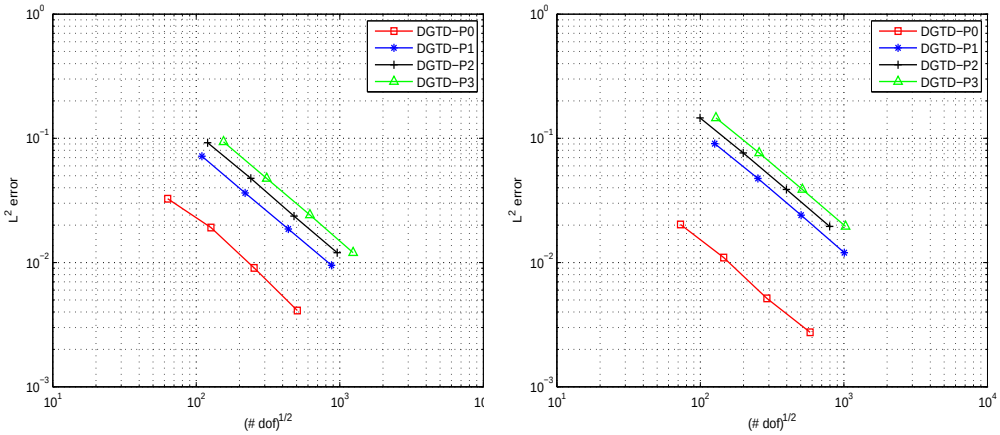

FIGURE 4.7. Rectangular PEC resonator with material interface. Numerical convergence of the h-refinement DGTD-$\mathbb{P}_p$ method. Conforming (left) and non-conforming (right) triangular meshes.

DGTD-$\mathbb{P}_p$: Conforming triangular mesh.				
Interpolation order p	**0**	**1**	**2**	**3**
Convergence order	1.00	0.98	0.98	0.99
DGTD-$\mathbb{P}_p$: Non-conforming triangular mesh.				
Interpolation order p	**0**	**1**	**2**	**3**
Convergence order	0.96	0.97	0.98	0.99

TABLE 4.4. Numerical convergence of the DGTD-$\mathbb{P}_p$ method.

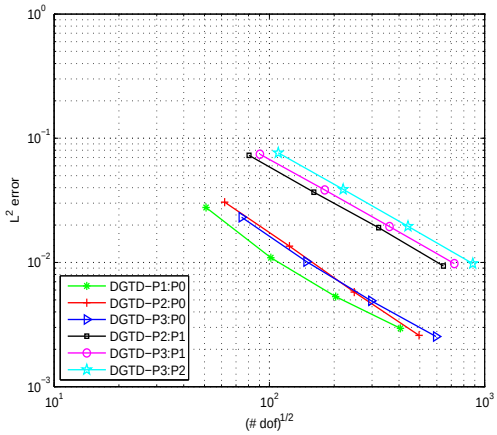

FIGURE 4.8. Rectangular PEC resonator with material interface. Numerical convergence of the hp-refinement DGTD-$\mathbb{P}_{p_c}$:$\mathbb{P}_{p_f}$ method. Non-conforming triangular meshes.

DGTD-$\mathbb{P}_{p_c}$:$\mathbb{P}_{p_f}$: Non-conforming triangular mesh.						
Interpolation orders p_c:p_f	**1:0**	**2:0**	**3:0**	**2:1**	**3:1**	**3:2**
Convergence order	1.07	1.20	1.07	0.98	0.98	1.00

TABLE 4.5. Numerical convergence of the DGTD-$\mathbb{P}_{p_c}$:$\mathbb{P}_{p_f}$ method.

4.3. Scattering of a plane wave by a dielectric cylinder. We consider now a typical problem, in which a plane wave impinges on a dielectric cylinder, experiencing reflection and refraction at the material interface. The geometry of the scenario is shown on Fig. 4.9.

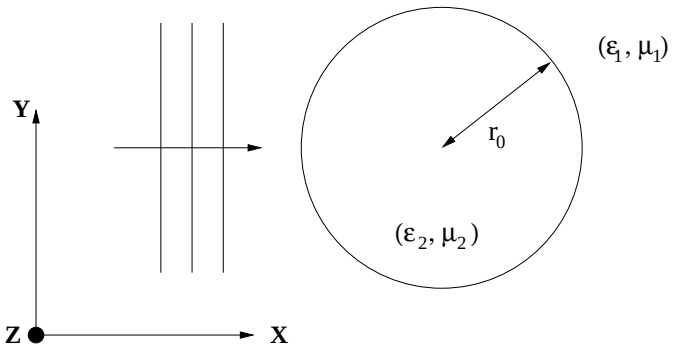

FIGURE 4.9. Scattering of a plane wave by a dielectric cylinder setting.

# dof	$\epsilon_2 = 3.25$, $\omega = \sqrt{20}\pi$		$\epsilon_2 = 6.625$, $\omega = \sqrt{8}\pi$	
	Error on (**E**,**H**)	Convergence order on (**E**,**H**)	Error on (**E**,**H**)	Convergence order on (**E**,**H**)
	DGTD-$\mathbb{P}_0$		DGTD-$\mathbb{P}_0$	
4000	1.28E−01	–	1.90E−01	–
16000	6.41E−02	1.00	9.25E−02	1.04
64000	3.20E−02	1.00	4.63E−02	1.00
256000	1.51E−02	1.08	2.30E−02	1.00
	DGTD-$\mathbb{P}_1$		DGTD-$\mathbb{P}_1$	
12000	2.72E−01	–	3.86E−01	–
48000	1.48E−01	0.87	2.07E−01	0.90
192000	7.87E−02	0.92	1.06E−01	0.96
768000	4.09E−02	0.94	5.39E−02	0.98
	DGTD-$\mathbb{P}_2$		DGTD-$\mathbb{P}_2$	
14400	3.84E−01	–	4.44E−01	–
57600	2.03E−01	0.92	2.38E−01	0.90
230400	1.01E−01	1.01	1.21E−01	0.97
921600	5.13E−02	0.98	6.12E−02	0.98
	DGTD-$\mathbb{P}_3$		DGTD-$\mathbb{P}_3$	
24000	3.93E−01	–	4.47E−01	–
96000	2.03E−01	0.95	2.38E−01	0.91
384000	1.03E−01	0.98	1.21E−01	0.97
1536000	5.15E−02	1.00	6.12E−02	0.98

TABLE 4.6. Rectangular PEC resonator with one material interface for different types of materials. The L^2 errors of the DGTD-$\mathbb{P}_p$ method at time $t = 1$.

DGTD-$\mathbb{P}_p$: Conforming triangular mesh.				
p	**0**	**1**	**2**	**3**
# dof	15200	180612	448980	774350
#Δt, CPU	110, 10	725, 449	1155, 1790	2350, 6269
DGTD-$\mathbb{P}_p$: Non-conforming triangular mesh.				
p	**0**	**1**	**2**	**3**
# dof	5621	511071	621390	1035500
# Δt, CPU	90, 3	1566, 3467	1974, 3383	3948, 11775
DGTD-$\mathbb{P}_{p_c}$:$\mathbb{P}_{p_f}$: Non-conforming triangular mesh.				
p_c:p_f	**1:0**	**2:0**	**2:1**	**3:1**
# dof	4092	7750	99312	127980
# Δt, CPU	96, 2	202, 8	648, 203	790, 310

TABLE 4.7. CPU time (seconds), # dof and # Δt to achieve an error of 2% at time $t = 1$.

We assume that the cylinder is illuminated by a monochromatic plane wave of the form:

$$E_z^{\text{inc}} = \exp(-\mathsf{i}(k_1 x - \omega t)), \quad H_y^{\text{inc}} = -\exp(-\mathsf{i}(k_1 x - \omega t)),$$

where $k_1 = \omega\sqrt{\epsilon_1\mu_1}$. In this case, the exact solution of the scattering problem is given by:

$$E_z(x,y,t) = E_z(r,\theta,t) = e^{\mathsf{i}\omega t}\begin{cases} \displaystyle\sum_{n=-\infty}^{\infty} C_n^{\text{tot}} J_n(k_2 r) e^{\mathsf{i}n\theta}, & r \le r_0, \\ \displaystyle\sum_{n=-\infty}^{\infty} (\mathsf{i}^{-n} J_n(k_1 r) + C_n^{\text{scat}} H_n^{(2)}(k_1 r)) e^{\mathsf{i}n\theta}, & r > r_0, \end{cases}$$

where J_n and $H_n^{(2)}$ represent the n-th order Bessel function of the first kind and the Hankel function of the second kind, respectively, and $k_2 = \omega\sqrt{\epsilon_2\mu_2}$ is the propagation constant for homogeneous, lossless dielectric medium. As usual, $(r,\theta) = (\sqrt{x^2+y^2}, \arctan(y/x))$ represent the usual polar coordinates. The expansion coefficients for the total field interior to the cylinder are:

$$C_n^{\text{tot}} = \mathsf{i}^{-n} \frac{(k_1/\mu_1) J_n'(k_1 r_0) H_n^{(2)}(k_1 r_0) - (k_1/\mu_1) H_n^{(2)'}(k_1 r_0) J_n(k_1 r_0)}{(k_2/\mu_2) J_n'(k_2 r_0) H_n^{(2)}(k_1 r_0) - (k_1/\mu_1)) H_n^{(2)'}(k_1 r_0) J_n(k_2 r_0)}.$$

The corresponding coefficients for the scattered field are:

$$C_n^{\text{scat}} = \mathsf{i}^{-n} \frac{(k_1/\mu_1) J_n'(k_1 r_0) J_n(k_2 r_0) - (k_2/\mu_2) J_n'(k_2 r_0) J_n(k_1 r_0)}{(k_2/\mu_2) J_n'(k_2 r_0) H_n^{(2)}(k_1 r_0) - (k_1/\mu_1) H_n^{(2)'}(k_1 r_0) J_n(k_2 r_0)}.$$

Using Maxwell's equations (2.1), one can recover the solutions for the magnetic field components. Then, the angular component of the total magnetic field is:

$$H_\theta(r,\theta,t) = -e^{\mathsf{i}\omega t}\begin{cases} \dfrac{-\mathsf{i}k_2}{\omega\mu_2} \displaystyle\sum_{n=-\infty}^{\infty} C_n^{\text{tot}} J_n'(k_2 r) e^{\mathsf{i}n\theta}, & r \le r_0, \\ \dfrac{-\mathsf{i}k_1}{\omega\mu_1} \displaystyle\sum_{n=-\infty}^{\infty} (\mathsf{i}^{-n} J_n'(k_1 r) + C_n^{\text{scat}} H_n^{(2)'}(k_1 r)) e^{\mathsf{i}n\theta}, & r > r_0, \end{cases}$$

and the radial component is:

$$H_r(r,\theta,t) = -e^{\mathsf{i}\omega t}\begin{cases} \dfrac{\mathsf{i}}{\omega\mu_2 r} \displaystyle\sum_{n=-\infty}^{\infty} \mathsf{i}n C_n^{\text{tot}} J_n(k_2 r) e^{\mathsf{i}n\theta}, & r \le r_0, \\ \dfrac{\mathsf{i}}{\omega\mu_1 r} \displaystyle\sum_{n=-\infty}^{\infty} \mathsf{i}n(\mathsf{i}^{-n} J_n(k_1 r) + C_n^{\text{scat}} H_n^{(2)}(k_1 r)) e^{\mathsf{i}n\theta}, & r > r_0. \end{cases}$$

We consider a situation already treated in [4]-[17]-[25] in which $\mu_1 = \mu_2 = \epsilon_1 = 1$, *i.e.* the material is non-magnetic, and the material exterior to the cylinder is assumed to be vacuum. The cylinder has a radius $r_0 = 0.6$ and bounds a material of relative permittivity $\epsilon_2 = 2.25$. The angular frequency is $\omega = 2\pi$ and the computational domain Ω is chosen as a cylinder of radius 1.5 m centered at $(0,0)$. In this special case, all three field components are continuous across the material interface. The first derivative of E_z is also continuous across the interface, but first derivatives of H_x and H_y are discontinuous. Regarding the boundary condition at

the artificial boundary of the computational domain, we use a first order Silver-Müller absorbing boundary condition. Contour lines of the E_z and H_y components at times $t = 1$ and $t = 10$ are shown on Fig. 4.10 for a calculation based on the conforming DGTD-$\mathbb{P}_1$ method.

To show the effectiveness of the *hp*-like method, we compare the DGTD-$\mathbb{P}_p$ method using conforming meshes with the DGTD-$\mathbb{P}_{p_c}$:$\mathbb{P}_{p_f}$ method using non-conforming meshes. To this end, we first construct a conforming mesh consisting of 11920 triangles and 6001 nodes and we use different cases of DGTD-$\mathbb{P}_p$ method, where the interpolation order p is uniform in all triangles of the mesh. Then, a non-conforming mesh is obtained by locally refining (two refinement levels) the cylindrical zone $0.55 \leq r \leq 0.65$ of a coarse conforming mesh. The resulting non-conforming mesh consists of 5950 triangles and 3151 nodes (300 of them are hanging nodes). Results are shown on Fig. 4.11 and 4.12 in terms of the x-wise 1D distribution along $y = 0.0$ m of the E_z and H_y components respectively. Table 4.8 summarizes the CPU time, the relative L^2 error, the number of time steps and the number of degrees of freedom for some configurations of the DGTD methods. As expected, the gain in CPU time between the proposed *hp*-like DGTD-$\mathbb{P}_{p_c}$:$\mathbb{P}_{p_f}$ and the conforming DGTD-$\mathbb{P}_p$ methods is considerable. For instance, to achieve an error level of 5%, the DGTD-$\mathbb{P}_2$:$\mathbb{P}_0$ scheme requires, on the one hand, 3 times less memory and 21 times less CPU time than the DGTD-$\mathbb{P}_2$ scheme and, on the other hand, 6 times less memory and 72 times less CPU time than the DGTD-$\mathbb{P}_3$ scheme. These gains are slightly lower if we increase the interpolation orders p_c and p_f, for instance, the DGTD-$\mathbb{P}_2$:$\mathbb{P}_1$ scheme requires 2.5 times less memory and 16 times less CPU time than the DGTD-$\mathbb{P}_2$ scheme while the DGTD-$\mathbb{P}_3$:$\mathbb{P}_2$ scheme requires 2.3 times less memory and 10 times less CPU time than the DGTD-$\mathbb{P}_3$ scheme.

The observed gains in memory usage and computing time are for a great part due to the fact that the CFL condition of the DGTD-$\mathbb{P}_{p_c}$:$\mathbb{P}_{p_f}$ is larger than the one for the DGTD-$\mathbb{P}_{p_c}$ ($p_c = p$) method, and the local refinement (in a non-conforming way) is only applied to regions where the solution is of low regularity (*i.e.* near the material interface), and in such region a low interpolation degree p_f (*e.g.* $p_f = 0$) is applied. Furthermore, a coarse mesh and a high interpolation degree p_c are used far from the material interface where the solution is smooth. Here, p_f is used in 55% of the triangles of the mesh. In the three-dimensional case, these gains could be larger than in the two-dimensional case, because the number of degrees of freedom increases faster with the polynomial order.

DGTD-$\mathbb{P}_p$: Conforming triangular mesh.				
p	**0**	**1**	**2**	**3**
L^2 error, CPU	13.6%, 20	7.15%, 178	5.20%, 542	5.22%, 1817
# dof, # Δt	11920, 3206	35760, 10687	71520, 16030	119200, 32060
DGTD-$\mathbb{P}_{p_c}$:$\mathbb{P}_{p_f}$: Non-conforming triangular mesh.				
p_c:p_f	**1:0**	**2:0**	**2:1**	**3:2**
L^2 error, CPU	11.6%, 9	5.36%, 25	5.39%, 33	5.37%, 179
# dof, # Δt	11450, 1621	19700, 2702	26100, 2702	46700, 8104

TABLE 4.8. L^2 error, CPU time (minutes), # dof and # Δt are measured at time $t = 5$.

5. Concluding remarks

In this paper we have studied discontinuous Galerkin methods for the discretization of the time-domain Maxwell equations on both conforming and non-conforming

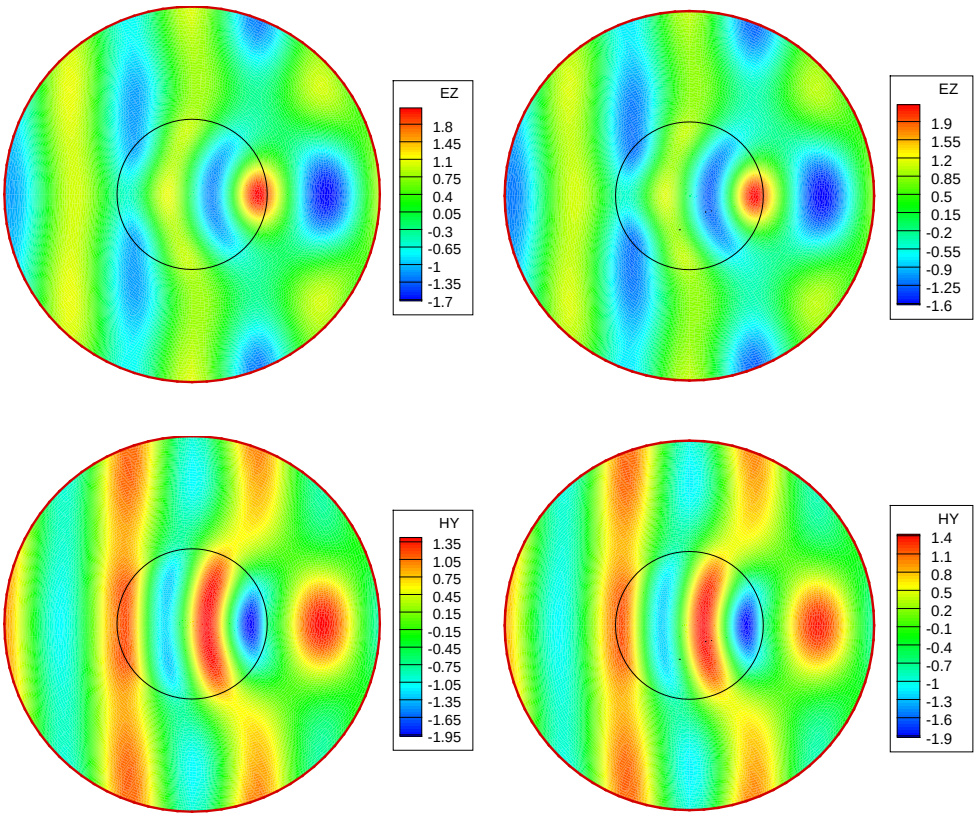

FIGURE 4.10. Scattering of a plane wave by a dielectric cylinder. Contour lines of E_z (top) and H_y (bottom) at times $t = 1$ (left) and $t = 10$ (right). DGTD-$\mathbb{P}_1$ method using a conforming mesh with 6001 nodes and 11920 triangles.

locally refined triangular meshes with arbitrary level hanging nodes. The proposed DGTD methods are non-dissipative and conserve a discrete form of the electromagnetic energy. A detailed numerical evaluation is presented for a series of wave propagation problems in homogeneous and heterogeneous media. We have shown that the proposed non-conforming DGTD-$\mathbb{P}_{p_c}$:$\mathbb{P}_{p_f}$ method, on the one hand, can reduce (or eliminate) the numerical dispersion error resulting from the conforming DGTD-$\mathbb{P}_p$ method with a reasonable cost and, on the other hand, is less expensive than the conforming DGTD-$\mathbb{P}_p$, particularly in the case of heterogeneous media.

This work is a first step towards the development of a non-conforming hp-adaptive method for solving the time-domain Maxwell equations. Concerning future works, a first objective will be to adapt the hp-like method proposed here to the 3D case. Indeed, the formulation of the method is straightforward, however, from the algorithmic and computational viewpoints, there are two difficulties: the generation of a non-conforming tetrahedral mesh and the evaluation of the non-conforming interface matrix $\mathbb{S}_{ik}$. As a first step, a local refinement will be done by splitting each tetrahedron into eight tetrahedra. The non-conforming interface matrix can be evaluated by using a cubature formula and we plan to use the points and weights

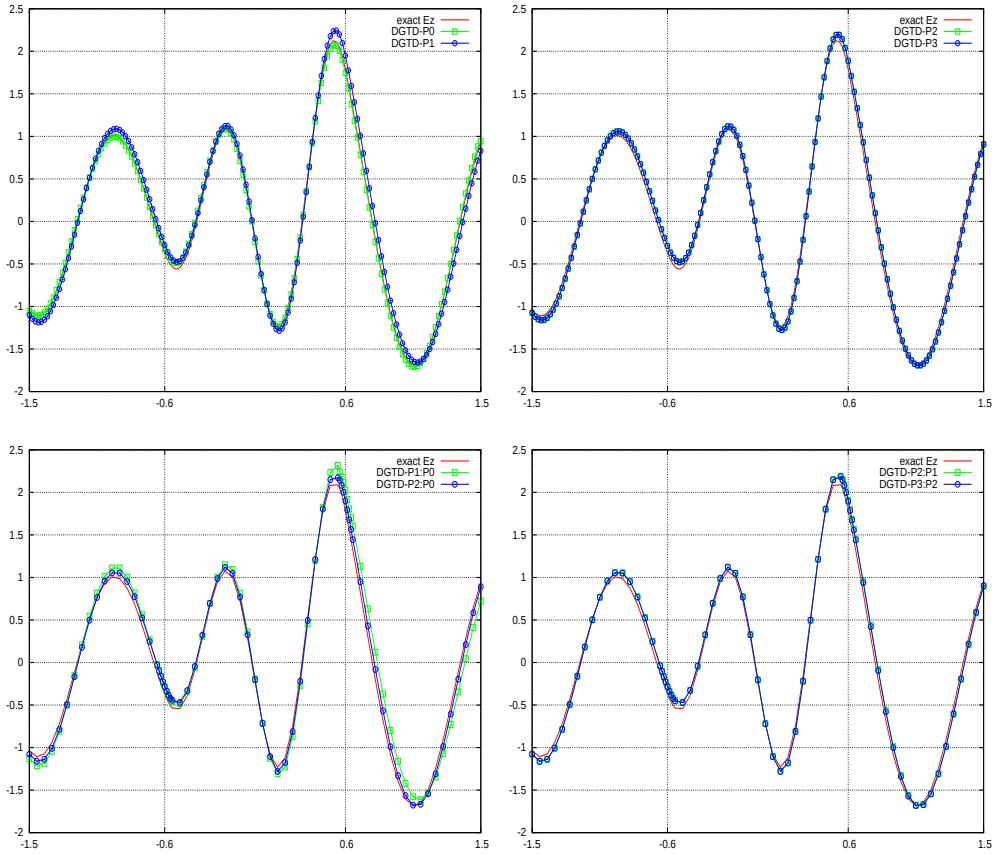

FIGURE 4.11. Scattering of a plane wave by a dielectric cylinder.
1D distribution of E_z along $y = 0.0$ at time $t = 5$.
DGTD-$\mathbb{P}_p$ method (top) and DGTD-$\mathbb{P}_{p_c}$:$\mathbb{P}_{p_f}$ (bottom).

of the cubature formulas proposed in [10]. A second important objective will be the design of an a posteriori error estimator to reduce both, the computing time and the memory usage.

On the other hand, a characteristic of our DGTD methods which can be improved is the time accuracy through the choice of an alternative explicit time integration scheme. Indeed, the leap-frog scheme used in this study is non-dissipative and second-order accurate. One possible approach to increase the accuracy is to apply a fourth-order leap-frog time scheme [35]-[27]. An expected advantage of this accuracy enhancement strategy is that it will preserve basic properties of the underlying second-order accurate scheme among which, stability and non-dissipativity.

Acknowledgment

The author would like to express his heartfelt gratitude to Loula Fezoui and Stéphane Lanteri for many helpful discussions during this work. The author also extends its sincere appreciation to Professor Jun Zou and to the anonymous referee for the helpful suggestions which have greatly improved the quality of this paper. This research was partially supported by a grant from the French National Ministry of Education and Research (MENSR, 19755-2005).

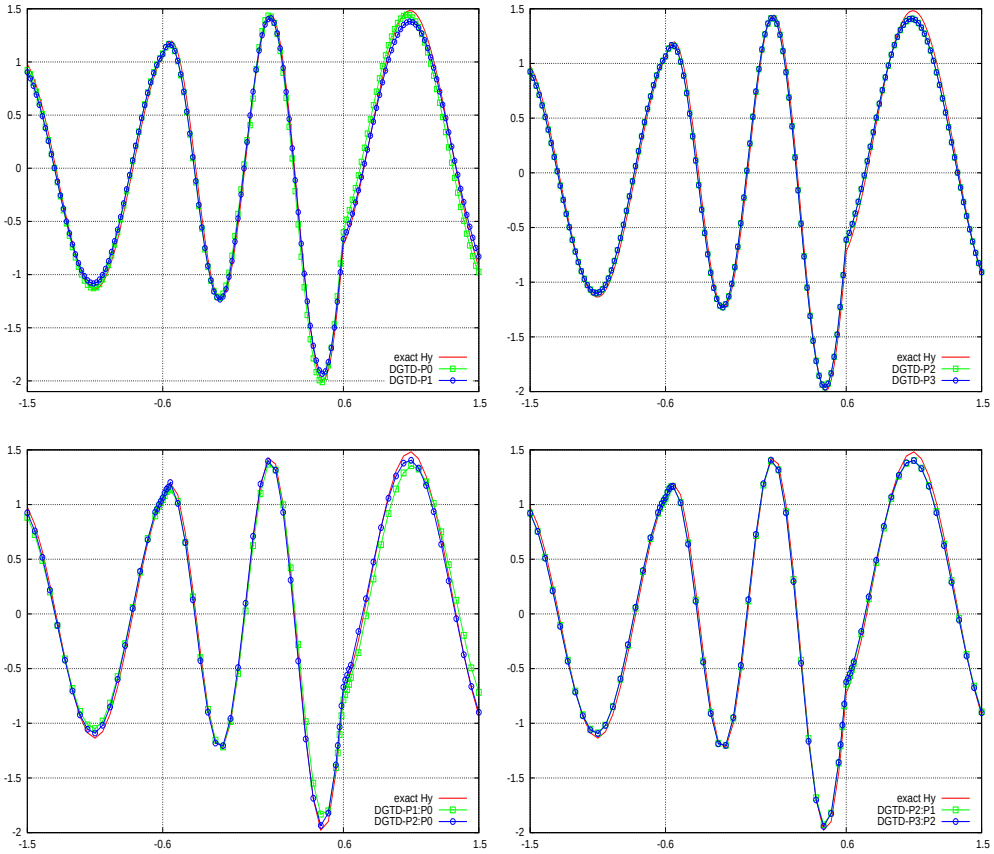

FIGURE 4.12. Scattering of a plane wave by a dielectric cylinder.
1D distribution of H_y along $y = 0.0$ at time $t = 5$.
DGTD-$\mathbb{P}_p$ method (top) and DGTD-$\mathbb{P}_{p_c}$:$\mathbb{P}_{p_f}$ (bottom).

References

[1] S. Abarbanel, A. Ditkowski and A. Yefet, Bounded error schemes for the wave equation on complex domains, J. Sci. Comput., 26(2006), 67-81.
[2] M. Bernacki, L. Fezoui, S. Lanteri and S. Piperno, Parallel unstructured mesh solvers for heterogeneous wave propagation problems, Appl. Math. Model., 30(2006), 744–763.
[3] A. Bossavit, Solving Maxwell equations in a closed cavity, and the question of spurious modes, IEEE Trans. Magnetics, 26(1990), 702–705.
[4] W. Cai and S. Deng, An upwinding embedded boundary method for Maxwell's equations in media with material interfaces: 2D case, J. Comput. Phys., 190(2003), 159–183.
[5] N. Canouet, L. Fezoui and S. Piperno, Discontinuous Galerkin time-domain solution of Maxwell's equations on locally-refined nonconforming cartesian grids, COMPEL, 24(2005), 1381–1401.
[6] B. Cockburn, G. E. Karniadakis and C. W. Shu, editors, Discontinuous Galerkin methods. Theory, computation and applications, vol. 11 of Lecture Notes in Computational Science and Engineering, Springer-Verlag, 2000.
[7] S. Cochez-Dhondt and S. Nicaise, Robust a posteriori error estimation for the heterogeneous Maxwell equations, Comput. Methods Appl. Mech. Engrg., 196(2007), 2583-2595.
[8] G. Cohen, X. Ferrieres and S. Pernet, A spatial high-order hexahedral discontinuous Galerkin method to solve Maxwell's equations in time domain, J. Comput. Phys., 217(2006), 340–363.
[9] F. Collino, T. Fouquet and P. Joly, Conservative space-time mesh refinement methods for the FDTD solution of Maxwell's equations, J. Comput. Phys., 211(2006), 9–35.
[10] R. Cools, An encyclopedia of cubature formulas, J. Complexity, 19(2003), 445-453.

[11] A. Ditkowski, K. Dridi and J. S. Hesthaven, Convergent cartesian grid methods for Maxwell's equations in complex geometries, J. Comput. Phys., 170(2001), 39–80.
[12] K. Dridi, J. S. Hesthaven and A. Ditkowski, Staircase-free finite-difference time-domain formulation for general materials in complex geometries, IEEE Trans. Antennas and Propagat., 49(2001), 749–755.
[13] H. Fahs, L. Fezoui, S. Lanteri and F. Rapetti, Preliminary investigation of a non-conforming discontinuous Galerkin method for solving the time domain Maxwell equations, IEEE Trans. on Magnet., 44(2008), 1254-1257.
[14] L. Fezoui, S. Lanteri, S. Lohrengel and S. Piperno, Convergence and stability of a discontinuous Galerkin time-domain method for the heterogeneous Maxwell equations on unstructured meshes, ESAIM: Math. Model. and Numer. Anal., 39(2005), 1149–1176.
[15] J. S. Hesthaven and T. Warburton, Nodal high-order methods on unstructured grids. I. Time-domain solution of Maxwell's equations, J. Comput. Phys., 181(2002), 186–221.
[16] J. S. Hesthaven, High-order accurate methods in time-domain computational electromagnetics, Adv. Imaging Electron Phys., 127(2003), 59–123.
[17] J. S. Hesthaven, P. G. Dinesen and J. P. Lynov, Spectral collocation time-domain modeling of diffractive optical elements, J. Comput. Phys., 155(1999), 287–306.
[18] E. Kashdan and E. Turkel, High-order accurate modeling of electromagnetic wave propagation across media: grid conforming bodies, J. Comput. Phys., 218(2006), 816–835.
[19] J. C. Nedelec, A new family of mixed finite elements in $\mathbb{R}^3$, Numer. Math., 50(1986), 57–81.
[20] A. C. Polycarpou, C. A. Balanis and A. Stefanov, Helicopter rotor-blade modulation of antenna radiation characteristics, IEEE Trans. Antennas and Propagat., 49(2001), 688–696.
[21] W. Rachowicz and A. Zdunek, An *hp*-adaptive finite element method for scattering problems in computational electromagnetics, Internat. J. Numer. Methods Engrg., 62(2005), 1226–1249.
[22] F. Reitich and K. K. Tamma, State-of-the-art, trends and directions in computational electromagnetics, Comput. Meth. Eng. Sci., 5(2004), 287–294.
[23] J.-F. Remacle, J. Flaherty and M. Shephard, An adaptive discontinuous Galerkin technique with an orthogonal basis applied to compressible flow problems, SIAM Review, 45(2003), 53–72.
[24] G. Scarella, O. Clatz, S. Lanteri, G. Beaume, S. Oudot, J.-P. Pons, S. Piperno, P. Joly and J. Wiart, Realistic numerical modelling of human head tissue exposure to electromagnetic waves from cellular phones, Comptes Rendus Physique, 7(2006), 501–508.
[25] Y. Shi, L. Li and C.-H. Liang, Two dimensional multidomain pseudospectral time-domain algorithm based on alternating-direction implicit method, IEEE Trans. Antennas and Propagat., 54(2006), 1207–1214.
[26] P. Solin, K. Segeth and I. Dolezel, Higher-order finite element methods, Chapman & Hall/CRC Press, Boca Raton, 2003.
[27] H. Spachmann, R. Schuhmann and T. Weiland, High order explicit time integration schemes for Maxwell's equations, Int. J. Numer. Model., 15(2002), 419-437.
[28] A. Taflove, Advances in computational electrodynamics, the finite-difference time-domain method, Artech House, Boston, London, 1998.
[29] E. Turkel and A. Yefet, Fourth order compact implicit method for the Maxwell equations with discontinuous coefficients, Appl. Numer. Math., 33(2000), 125–134.
[30] E. Turkel and A. Yefet, On the construction of a high order difference scheme for complex domains in a cartesian grid, Appl. Numer. Math., 33(2000), 113–124.
[31] T. Xiao and Q. H. Liu, A staggered upwind embedded boundary (SUEB) method to eliminate the FDTD staircasing error, IEEE Trans. Antennas and Propagat., 52(2004), 730–741.
[32] Z. Xie, C.-H. Chan and B. Zhang, An explicit fourth-order orthogonal curvilinear staggered-grid FDTD method for Maxwell's equations, J. Comput. Phys., 175(2002), 739–763.
[33] K. S. Yee, Numerical solution of initial boundary value problems involving Maxwell's equations in isotropic media, IEEE Trans. Antennas and Propagat., 14(1966), 302–307.
[34] A. Yefet and P. G. Petropoulos, A staggered fourth-order accurate explicit finite difference scheme for the time-domain Maxwell's equations, J. Comput. Phys., 168(2001), 286–315.
[35] J. L. Young, High-order, leapfrog methodology for the temporally dependent Maxwell's equations, Radio Sci., 36(2001), 9-17.
[36] S. Zhao and G. W. Wei, High-order FDTD methods via derivative matching for Maxwell's equations with material interfaces, J. Comput. Phys., 200(2004), 60–103.

INRIA, Nachos team, 2004 Route des Lucioles, BP 93, F-06902 Sophia-Antipolis Cedex, France
E-mail: Hassan.Fahs@gmail.com